Article

Gamma Radiation Synthesis of Ag/P25 Nanocomposites for Efficient Photocatalytic Degradation of Organic Contaminant

Zihua Zeng [†], Shuangxiao Li [†], Xueyan Que, Jing Peng [ID], Jiuqiang Li and Maolin Zhai *

Beijing National Laboratory for Molecular Sciences, Radiochemistry and Radiation Chemistry Key Laboratory of Fundamental Science, The Key Laboratory of Polymer Chemistry and Physics of the Ministry of Education, College of Chemistry and Molecular Engineering, Peking University, Beijing 100871, China
* Correspondence: mlzhai@pku.edu.cn
† These authors contributed equally to this work.

Abstract: Titanium dioxide (TiO_2) has garnered significant attention among various photocatalysts, whereas its photocatalytic activity is limited by its wide bandgap and inefficient charge separation, making the exploration of new strategies to improve its photocatalytic performance increasingly important. Here, we report the synthesis of Ag/P25 nanocomposites through a one-step gamma-ray radiation method using $AgNO_3$ and commercial TiO_2 (Degussa P25). The resulting products were characterized by powder X-ray diffraction, UV-Vis diffused reflectance spectroscopy, transmission electron microscopy, and X-ray photoelectron spectroscopy. The effect of free radical scavengers, feed ratios of Ag/P25, and dose rates on the photocatalytic activity of the Ag/P25 nanocomposites were systematically investigated using rhodamine B under Xenon light irradiation. The results showed that the Ag/P25 photocatalyst synthesized with a feed ratio of 2.5 wt% and isopropyl alcohol as the free radical scavenger at a dose rate of 130 Gy/min exhibited outstanding photocatalytic activity, with a reaction rate constant of 0.0674 min^{-1}, much higher than that of P25. Additionally, we found that the particle size of Ag could be effectively controlled by changing the dose rate, and the Ag/P25 nanocomposites doped with smaller size of Ag nanoparticles performed higher photocatalytic activities. The synthesis strategy presented in this study offers new insight into the future development of highly efficient photocatalysts using radiation techniques.

Keywords: Ag/P25 nanocomposites; gamma-ray radiation method; photocatalytic performance

1. Introduction

Environmental protection has become an urgent and crucial concern nowadays in the face of increased organic and inorganic pollutants in the natural environment due to rapid industrialization [1,2]. The consequences of this pollution pose a significant threat to human health, social stability, and sustainability [3,4]. Consequently, there has been a surge of research in both academic and industrial settings toward reducing environmental pollution from organic and inorganic pollutants. The challenge lies in finding simple, eco-friendly, and effective techniques to remove contaminants [5].

Advanced oxidation processes (AOPs) are a series of chemical treatment for water or wastewater aimed at removing organic contaminants by oxidation. AOPs rely on the in situ generation of highly reactive oxidants, in particular, hydroxyl radical (OH·), which can oxidize virtually any compound in water [6]. The applications of AOPs in the treatment of a wide range of organic pollutants such as industrial dyes, pesticides, and fertilizers, have shown high reaction rate constants and excellent removal efficiency [7,8]. Photocatalysis, as a process technology which has been investigated for use as a kind of AOPs, has emerged as a promising and eco-friendly method, owing to its energy-saving, environmentally friendly, and highly efficient properties [9–11]. During the photocatalytic process, reactive oxygen species (ROS) are generated from electron capture by oxygen and water oxidation, such as

superoxide ($O_2{}^-$) and OH·, which will engage in subsequent oxidation–reduction reactions as highly reactive oxidants [12]. Unlike activated carbon adsorption or membrane filtration methods, photocatalysis can achieve complete degradation of organic and inorganic pollutants through a series of oxidation–reduction reactions [13,14].

Photocatalysts play a crucial role in the photocatalytic process since they greatly affect the absorbance spectrum and the electron–hole separation efficiency, which ultimately determines the photocatalytic efficiency [15]. Semiconductors have been extensively studied as photocatalysts because of their unique energy band structures and their ability to contain inequal numbers of electrons and holes [16,17]. The P-type semiconductors contain an excess of holes, while the N-type semiconductors are abundant of electrons. As a N-type semiconductor, titanium dioxide (TiO_2) has garnered significant attention due to its low cost, easy commercial availability, nontoxicity, high thermal and photochemical stability, and unique optical properties [18,19]. TiO_2 exists in various nanoscale forms, including nanospheres [20], nanowires [21,22], nanotubes [23], nanofibers [24], and has found wide-ranging applications in pollutant degradation [25,26], hydrogen production [27,28], and carbon dioxide reduction [29], etc. However, the large band gap width of TiO_2 (3.0–3.2 eV) restricts its light absorption to the UV region and limits its use in visible light irradiation [13,30]. Additionally, TiO_2 exhibits fast recombination of photogenerated charges, which decreases the generation of ROS, lowers the photocatalytic quantum yield for OH· radical production, and hence hampers its practical application in photocatalysis [31].

To overcome these challenges, researchers have employed a range of specific surface modifications, including doping with non-metallic or metallic elements [27,32–35] and compounding with other semiconductors [14,36,37]. Moreover, the Z-scheme, a conceptual model in photosynthesis, has inspired researchers to design heterostructures and hybrid systems to preserve photogenerated electrons and holes with higher redox potentials and improve photocatalytic performance [38]. Among these modification methods, doping noble metal nanoparticles onto the surface of TiO_2 has proven particularly effective because the doped metal nanoparticles usually have high Schottky barriers, functioning as electron traps to enhance electron–hole separation and inhibit recombination of electrons and holes at the same time [39,40]. Additionally, the localized surface plasmon resonance (LSPR) effect triggered by the doped metal nanoparticles reduces the band gap width of metal-modified TiO_2, extending its absorption range into the visible light spectrum [41,42]. Silver (Ag) nanoparticles offer advantages over other noble metals, including ease of availability, excellent conductivity [43], and anti-bacterial properties [44]. Recent studies have focused on controlling the shapes and sizes of metal nanoparticles, including Ag. Under certain experimental conditions, the size of Ag nanoparticles can be controlled [45,46], influencing the LSPR effect, similar to other metals such as platinum [47], aurum [48], and ruthenium [49].

Various techniques have been developed to prepare Ag/TiO_2 nanocomposites, including photoreduction [50], sol-gel [51], solvothermal and hydrothermal treatment [52–56], as well as plasmonic fabrication [57–60]. In the field of water purification, extensive studies have demonstrated that Ag/TiO_2 nanocomposites can be applied to photodegrading organic dyes such as rhodamine B (RhB). Liang et al. synthesized Ag/TiO_2 nanocomposites under UV light irradiation and proposed different mechanisms of selective oxidation of RhB under UV or visible light [61]. Zhou et al. fabricated heterostructured Ag/g-C_3N_4/TiO_2 ternary photocatalyst through thermal oxidation etching process to form g-C_3N_4/TiO_2 and photoreduction process to load Ag nanoparticles on it. The as-synthesized photocatalyst showed a reaction rate constant of 0.0179 min^{-1} when degrading RhB under visible light, and high recycling stability [62]. As a matter of fact, the synthesis of the aforementioned Ag/TiO_2 nanocomposites necessitates intricate experimental conditions or relatively elaborate procedures. For instance, both solvothermal and hydrothermal treatments demand the sample to be heated above 180 °C for 5–10 h, while plasmonic fabrication requires intricate pretreatment to establish a suitable atmosphere for plasma treatment.

Radiation synthesis, however, presents a promising technology for synthesizing Ag/TiO$_2$ nanocomposites in aqueous solutions, since it is a clean, simple one-step, and highly effective method [63]. In the gamma-irradiation process, both oxidative and reductive species are generated such as electrons, H· and OH· radicals, where OH· radicals perform strong oxidative property, while the electrons and H· radicals possess the reductive potential to reduce Ag(I) [64,65]. This process can be carried out at room temperature without side reaction products, and the radiation chemical yield of those reductive species can usually achieve a high value, indicating its high efficiency. A free radical scavenger, which can prevent oxidative radicals from oxidizing the reduced Ag nanoparticles and reduce excess of reductive radicals, is essential to this method. Most common used free radical scavengers are alcohols (i.e., isopropyl alcohol [49], tert-butyl alcohol [66], and ethanol glycol [67]) and formic acid [68], and imidazolium-based ionic liquids also have diverse applications due to their high radiation stability [69]. Additionally, the irradiation dose rate plays an important role in radiation synthesis, since different dose rates affect the size of nanoparticles during their formation [63], and Ag particle size is controllable by changing different dose rate. To date, there have been few studies on the radiation synthesis of Ag/TiO$_2$ nanocomposites, particularly with regard to how dose rate influences the photocatalytic activities.

Here, we report the synthesis of Ag/P25 nanocomposites through a one-step gamma-ray radiation method using AgNO$_3$ and commercial TiO$_2$ (Degussa P25). Rhodamine B was selected as the model organic contaminant to investigate the photocatalytic performances of the resulting Ag/P25 nanocomposites under Xenon light irradiation. The effect of Ag/P25 feed ratio, dose rate, and different free radical scavengers on photocatalytic activity and the related mechanism were both discussed.

2. Materials and Methods

2.1. Materials

TiO$_2$ (P25, Degussa, Germany), silver nitrate (AgNO$_3$, AR, Xilong Scientific Co., Ltd., Shantou, China), isopropyl alcohol (IPA, AR, Beijing TongGuang Fine Chemicals Company, Hebei, China), ethylene glycol (EG, AR, Concord, Tianjin, China), 1-ethyl-3-methylimidazolium acetate (EMImAc, 99%, Energy Chemical, Shanghai, China), rhodamine B (RhB, AR, Macklin, China). All reagents were used as received without further purification.

2.2. Synthesis of Ag/P25 Nanocomposites

Ag/P25 nanocomposites were synthesized through a one-step gamma-ray radiation reduction method. In detail, 200 mg P25 powders were added to a mixed solution of IPA and pure water (1:9, v/v, 40 mL in total). The resulting suspensions were sonicated for 30 min to make P25 powders evenly dispersed. Different volumes of AgNO$_3$ solution (0.020 mol/L) were injected into the as-prepared suspensions to form a series of hybrid solutions with different feed ratios of Ag to P25 (0.5 wt%, 1.0 wt%, 2.5 wt%, and 5.0 wt%, respectively). The samples were then bubbled with nitrogen for 10 min to remove oxygen, sealed, and irradiated by gamma-ray from a ^{60}Co radiation source (Department of Applied Chemistry of Peking University). The absorbed dose was fixed at 28 kGy with different dose rates (7.2 Gy/min, 31 Gy/min, and 130 Gy/min). The products were subsequently centrifuged, washed with pure water several times, and finally lyophilized for three days. Two additional samples were synthesized under the conditions of 2.5 wt% Ag/P25 mass ratio and a dose rate of 31 Gy/min, with the pre-solutions mixed with 1.0327 g ionic liquid EMImAc (1 mL) and 39 mL pure water, or EG and pure water (1:2, v/v, 40 mL in total). The postprocessing of products remained unchanged. The abbreviations of the prepared samples and details of their synthesis are listed in Table 1.

2.3. Characterization

The phase compositions were analyzed by powder X-ray diffraction (XRD, PANalytical, Netherland, X-Pert3 Powder) with Cu Kα radiation (λ = 1.5418 Å). The X-ray

photoelectron spectroscopy (XPS) spectra were recorded on the AXIS Supra X-ray photo-electron spectrometer (Kratos Analytical, Manchester, UK) with an exciting source of Al Kα, using adventitious carbon (C 1s = 284.80 eV) as the calibration reference. The UV-vis diffuse reflectance spectra were measured by a UV-3600 Plus ultraviolet-visible-NIR spectrometer (Shimadzu, Nagoya, Japan) with the wavelength ranging from 200 to 800 nm. The micro morphologies of the catalysts were studied by field emission high-resolution transmission electron microscopy (HRTEM, JEOL, Tokyo, Japan, JEM-2100) at an acceleration voltage of 200 kV. The actual mass ratios of Ag in catalysts were characterized by inductively coupled plasma-optical emission spectrometry (ICP-OES, Leeman, Northern Outagamie County, WI, USA, Prodigy 7).

Table 1. Sample abbreviations and corresponding synthesis details.

Sample	Feed Ratio (Ag/P25 wt%)	Dose Rate (Gy/min)	Free Radical Scavenger
P25	0	/	/
Ag/P25-1	0.5	31	IPA
Ag/P25-2	1.0	31	IPA
Ag/P25-3	2.5	31	IPA
Ag/P25-4	5.0	31	IPA
Ag/P25-5	2.5	7.2	IPA
Ag/P25-6	2.5	130	IPA
Ag/P25-7	2.5	31	EMImAc
Ag/P25-8	2.5	31	EG

2.4. Measurements of Photocatalytic Activities

The photocatalytic activity of the Ag/P25 nanocomposites was estimated by the photodegradation of RhB (as the target pollutant) under Xenon light irradiation. To this end, a 100 mL jacketed beaker was used as the photoreactor. In the typical experiment, 30 mg catalyst was dispersed in the beaker containing a 90 mL aqueous solution of 30 mg/L RhB (pH = 5.5~6.5). The suspension was sonicated for 5 min and stirred for 55 min in the dark to reach an absorption–desorption equilibrium of RhB. Subsequently, the mixed suspension was exposed to Xenon light irradiation for 90 min while the distance between the lamp and the top surface of the suspension remained unchanged. At predetermined time intervals, a 2.5 mL aliquot was drawn out from the suspension and filtered by a 0.22 μm Nylon filter. Afterward, the transparent solution was transferred to a quartz cuvette and analyzed by UV-Vis absorption spectroscopy in a wavelength range from 450 nm to 600 nm. The concentration of RhB was determined by the absorbance at the wavelength of 554 nm, in accordance with the Lambert–Beer's Law. To investigate the photocatalytic recycling stability of the catalyst, a 12 mg sample was added to a 36 mL aqueous solution of 30 mg/L RhB. The suspension was irradiated with the Xenon light for 60 min. After filtration and washing, the catalyst was retrieved and added to another RhB solution with the same conditions, and this process was repeated three times. In this photocatalytic process, only the initial and final concentrations were measured to calculate the removal percentage of RhB in the solution.

The degradation rates of RhB with Ag/P25 nanocomposites are calculated by the following formula:

$$\text{Degradation (\%)} = (c_0 - c_t)/c_0 \times 100 = (A_0 - A_t)/A_0 \times 100, \tag{1}$$

where c_0 is the initial concentration of RhB solution and c_t is the corresponding concentration of RhB solution at time t, A_0 is the initial absorbance of RhB solution and A_t is the corresponding absorbance of RhB solution at time t. The reaction rate constant k is calculated based on a pseudo-first order kinetics [61] from the following equation:

$$-\ln(A_t/A_0) = -\ln(c_t/c_0) = kt. \tag{2}$$

3. Results and Discussion

3.1. Synthesis and Characterizations of Ag/P25 Nanocomposites

Ag/P25 nanocomposites were synthesized through a simple one-step gamma-ray induced reduction method, as illustrated in Figure 1. After being irradiated by gamma-ray from ^{60}Co source, Ag(I) was reduced to Ag nanoparticles (NPs) and doped on the surface of P25. The conversion to Ag NPs is confirmed by PXRD results. As shown in Figure 2, the peak at 44.3° can be attributed to (200) crystal plane of the cubic Ag phase (04-0783) of Ag/P25-4. The weak intensity of the Ag diffraction peak in Ag/P25-1 was due to the small amount of AgNO$_3$ precursor added, and the detection limitation of the PXRD technique. The ICP-OES results presented in Table 2 provide the actual mass ratios of Ag/P25 for the samples, which demonstrate an increase corresponding to the feed ratios of Ag/P25. Notably, when the sizes of Ag NPs are similar (1~3 nm), their actual amounts also show a proportionality to their respective feed ratios [70]. Furthermore, under the conditions studied, the doping efficiency of Ag on P25 consistently exceeds 70%, thereby indicating the efficiency of the method.
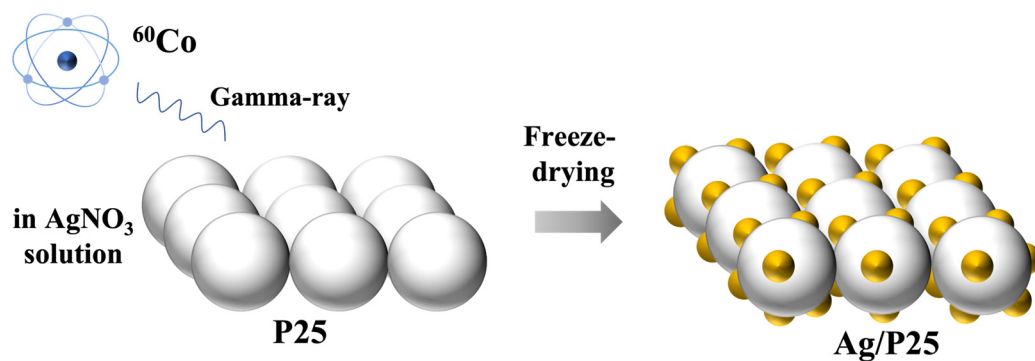

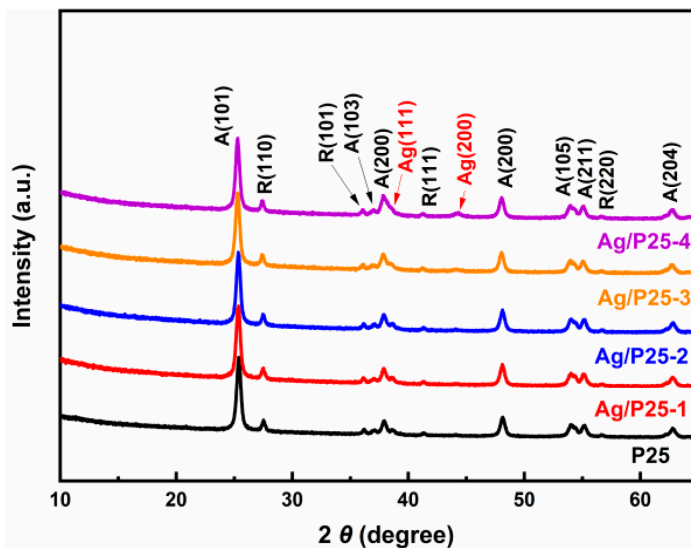**Figure 1.** Schematic illustration of the one-step synthesis of Ag/P25 nanocomposites.

Figure 2. PXRD patterns of Ag/P25 nanocomposites of different Ag/P25 feed ratios. A: anatase TiO$_2$ (21-1272); R: rutile TiO$_2$ (21-1276); Ag: cubic silver (04-0783).

To further confirm the elementary components of the catalysts and the valence state of Ag inside, XPS spectra of Ag/P25-6 are obtained and shown in Figure 3. The survey scans of XPS spectra (Figure 3a) indicate that Ag/P25 nanocomposites mainly consist of Ag, Ti, O, C, and no other elements, which is consistent with the results of PXRD. The XPS spectrum of C 1s (not shown) is used for the purpose of the drift correction of other elements. The XPS spectrum of Ag 3d in Figure 3b shows fitted peaks at 373.3 eV and 367.3 eV, which are

ascribed to Ag^0 $3d_{3/2}$ and Ag^0 $3d_{5/2}$, respectively. These two peaks with a 6.0 eV splitting confirm the existence of metallic Ag particles on P25 through the reduction of Ag^+ during the irradiation process. The fitted peaks corresponding to Ag^+ may be attributed to the partial oxidation of metallic silver particles, which is inevitable for the resultant samples in contact with air.

Table 2. ICP-OES results of samples with different Ag/P25 feed ratios.

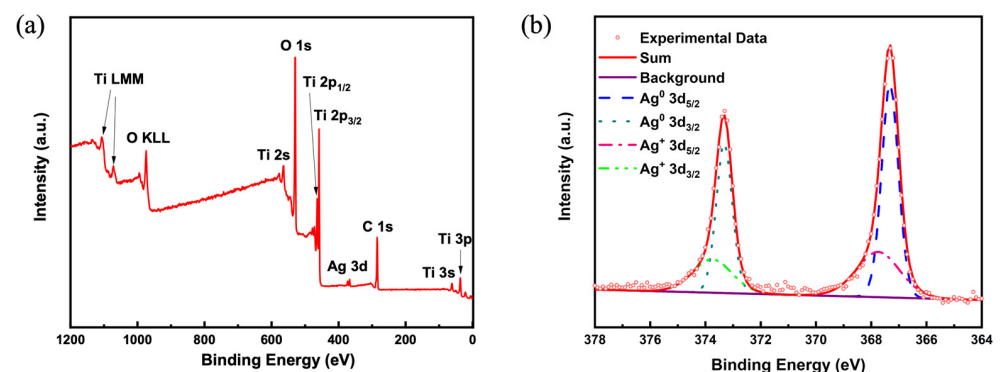| Sample	Feed Ratio (Ag/P25 wt%)	Ag (wt%)	Doping Efficiency (%)
Ag/P25-1	0.5	0.37	74
Ag/P25-2	1.0	0.71	71
Ag/P25-3	2.5	2.18	87
Ag/P25-4	5.0	4.22	84

Figure 3. (**a**) XPS spectra survey scan of Ag/P25-6; (**b**) Ag 3d XPS spectrum of Ag/P25-6.

TEM measurements were applied to detect the distribution and particle size of Ag NPs of Ag/P25 nanocomposites. TEM images in Figure 4a–c reveal that Ag NPs were loaded on the surface of P25 after gamma-ray irradiation, and that these Ag NPs at different dose rates are similar in shapes and locations but differ in particle size distributions. Figure 4d–f show the average diameters of Ag NPs of Ag/P25-5, Ag/P25-3, and Ag/P25-6. As the dose rate increases from 7.2 Gy/min, 31 Gy/min to 130 Gy/min, the average particle sizes decrease from 2.05 nm, 1.85 nm to 1.52 nm, respectively, and it is highly intuitive to notice that fewer outstanding large clusters of Ag NPs are observed under a higher dose rate. The morphology of Ag/P25 nanocomposites was examined by HRTEM, as shown in Figure 5. The lattice spacings of 0.35 nm and 0.24 nm match the crystal lattices of TiO_2 and Ag and can be attributed to anatase TiO_2 (101) and cubic Ag (111) species, respectively. Furthermore, the elemental mapping pictures of Ag/P25-6 (shown in Figure 4g–i) confirm the presence of the small dopped dots as Ag NPs.

The band gap width between the valence band and conduction band of a semiconductor material is a crucial parameter because it determines the potential energy difference between the electrons and the holes, which can be measured from the UV-Vis diffuse reflectance (DR) spectra. Figure 6 shows the UV-Vis DR spectra of P25 and different catalysts with various amounts of Ag and free radical scavengers. The cutting-line method is a common band gap calculation method whose principle is that the band edge wavelength λ_g is determined by the band gap width E_g, $E_g = 1240/\lambda_g$ (nm) [71]. The x value of the tangent of the absorbance curve intersected with the x-axis is recorded as the band edge wavelength λ_g. UV-Vis DR spectrum of P25, shown in Figure 6b, exhibits an absorption band at $\lambda_g = 400$ nm, indicating its band gap width of 3.10 eV, which is consistent with previous research [72]. For Ag/P25 photocatalysts prepared at different Ag/P25 feed ratios shown in Figure 6c–f, there are other wide absorption bands centered at 490–515 nm. The appearance of these absorption bands in the visible light range can be attributed to the LSPR effect of Ag NPs doped on the surface of P25. As the feed ratio of Ag/P25 increases, both the peak intensity and half width increase, indicating that higher concentrations of

silver nitrate led to the formation of more clusters of Ag NPs. On the other hand, the band gap widths of catalysts decrease with increasing Ag content because of the enhancement of the LSPR effect. For catalysts synthesized with different free radical scavengers, their band gap widths are smaller than P25, and band edge wavelengths extend to the visible light range, which can be attributed to the doped Ag NPs [27,42].
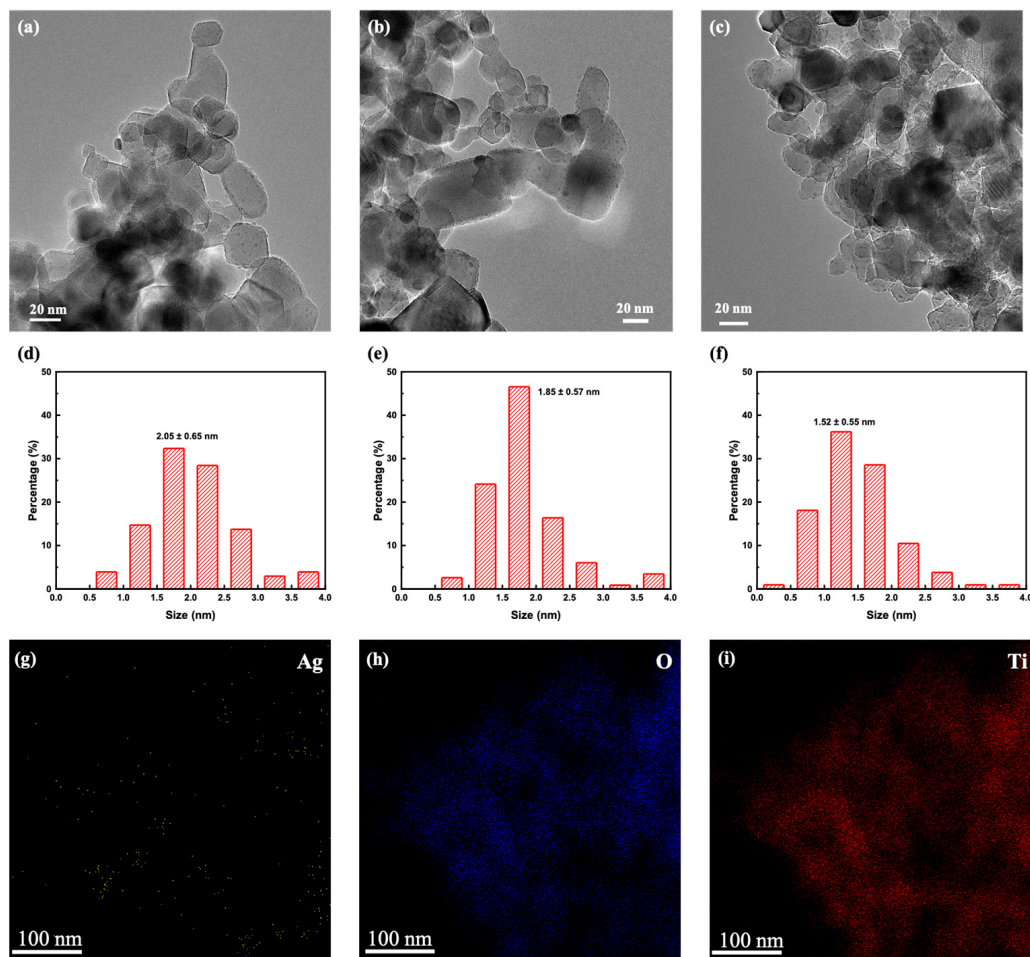

Figure 4. TEM images of Ag/P25 nanocomposites prepared at different dose rates and their corresponding particle size histograms: Ag/P25-5 (**a**,**d**); Ag/P25-3 (**b**,**e**); Ag/P25-6 (**c**,**f**); (**g**–**i**) the elemental mappings of Ag/P25-6 of Ag, O, Ti, respectively.
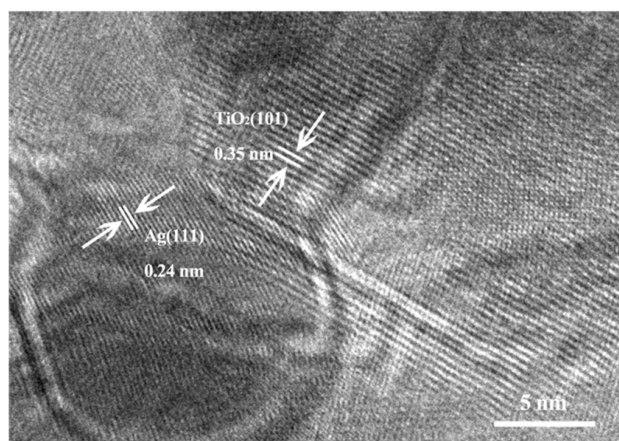

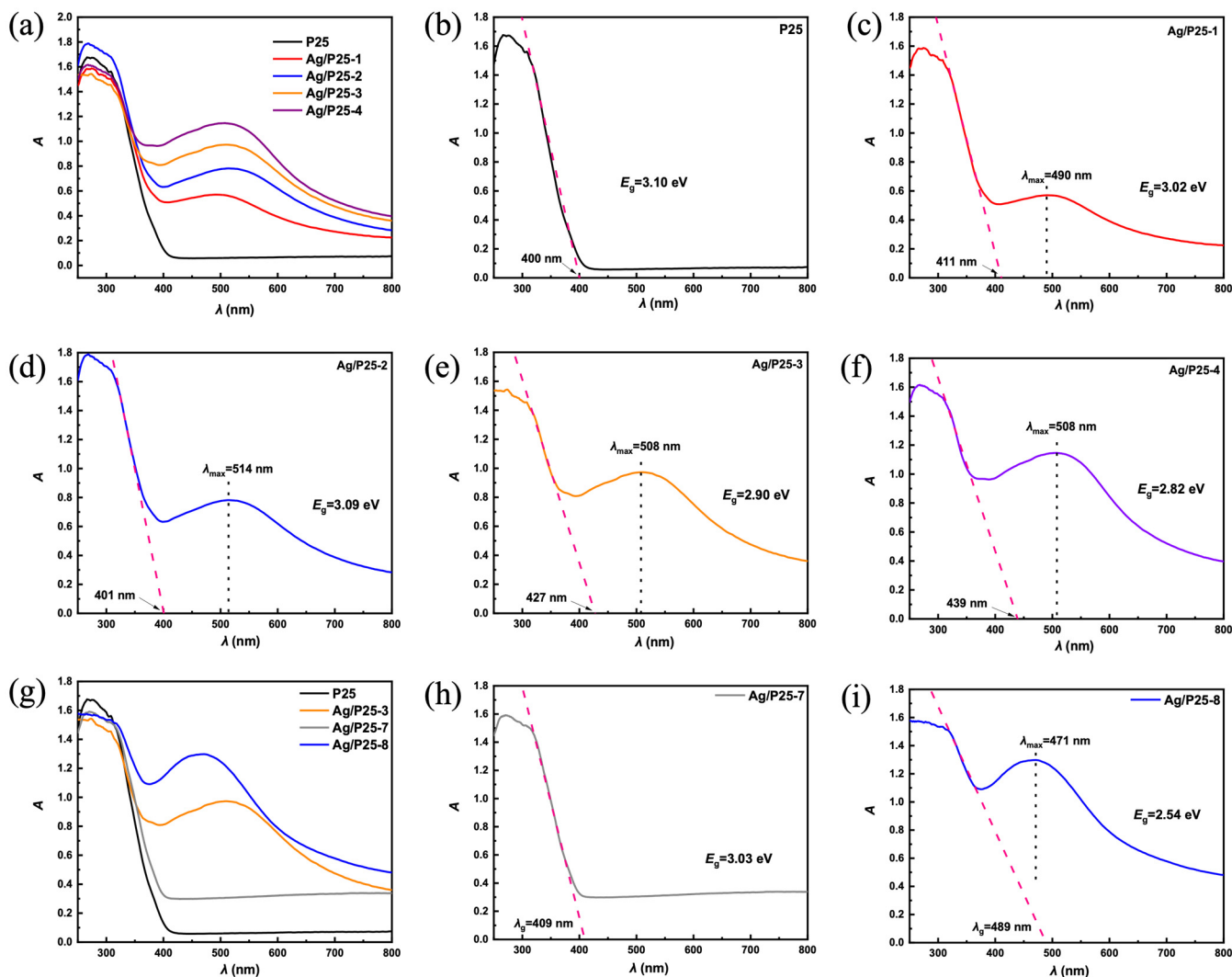**Figure 5.** HRTEM image of Ag/P25-3.

Figure 6. UV-Vis DR spectra of: (**a**,**g**): P25 and as-prepared Ag/P25 nanocomposites; (**b**): P25; (**c**–**f**): Ag/P25 nanocomposites synthesized at different feed ratios, Ag/P25-1, Ag/P25-2, Ag/P25-3, and Ag/P25-4, respectively; (**h**,**i**): Ag/P25 nanocomposites synthesized with different free radical scavengers, EMImAc, EG.

3.2. Photocatalytic Activities

The photocatalytic performances of the as-prepared Ag/P25 nanocomposites were measured under Xenon light ($\lambda > 200$ nm). Figure 7 illustrates the changes in UV-Vis absorption spectra of RhB solutions in the presence of P25 and Ag/P25-4 at predetermined times. The dotted arrow indicates the blue shift in the maximum absorption wavelength (λ_{max}) of RhB solutions during the photodegradation, which implies the de-ethylation process of RhB [39]. Previous studies by Natarajan et al. [73] and Liang et al. [61] have reported that λ_{max} of the oxidation products of RhB under UV and visible light irradiation are gradually decreasing though the de-ethylation process. The RhB solutions with catalysts can reach the absorption–desorption equilibrium in the dark for 60 min, and almost complete degradation of RhB molecules was achieved after a 60-min Xenon light irradiation.

The photocatalytic degradation curves of RhB (c/c_0 vs. irradiation time) are presented in Figure 8a,d,g, revealing that the degradation rates of RhB with Ag/P25 nanocomposites (calculated based on Equation (1)) are higher than that with P25. A pseudo-first order kinetics fitting (Equation (2)) is performed to draw the plots of $-\ln(c/c_0)$ vs. irradiation time and determine the reaction rate constant k. The corresponding plots of photocatalysts synthesized with different free radical scavengers, Ag/P25 feed ratios, and dose rates are

depicted in Figure 8b,e,h and Figure 8c,f,i, respectively. The squared correlation coefficients of linear fitting are all greater than 0.985, indicating that there is a strong linear relationship between $-\ln(c/c_0)$ and irradiation time, and that the variation of $-\ln(c/c_0)$ versus time is in accordance with the first order reaction. Applying IPA, EMImAc, and EG as different free radical scavengers in Ag/P25-3, Ag/P25-7, and Ag/P25-8, the order of their rate constants is Ag/P25-3>Ag/P25-7>Ag/P25-8. Therefore, isopropyl alcohol is selected to act as the free radical scavenger in further studies of this work. With Ag/P25 feed ratios increasing from 0.5%, 1.0%, 2.5% to 5.0%, the rate constants first increase and then decrease, reaching the peak at 2.5 wt% Ag/P25 feed ratio, and they are better than that of P25. This result indicates that Ag NPs significantly influence the photocatalytic activities of Ag/P25 nanocomposites. Regarding the influence of different dose rates, the rate constants of Ag/p25-5, Ag/P25-3, and Ag/P25-6 become greater while the dose rates increase from 7.2 Gy/min to 130 Gy/min. Among the eight synthesized Ag/P25 nanocomposites, Ag/P25-6 exhibits the best photocatalytic performance under Xenon light irradiation, with a rate constant of 0.0674 min^{-1}, which is 2.1 times higher than that of P25.
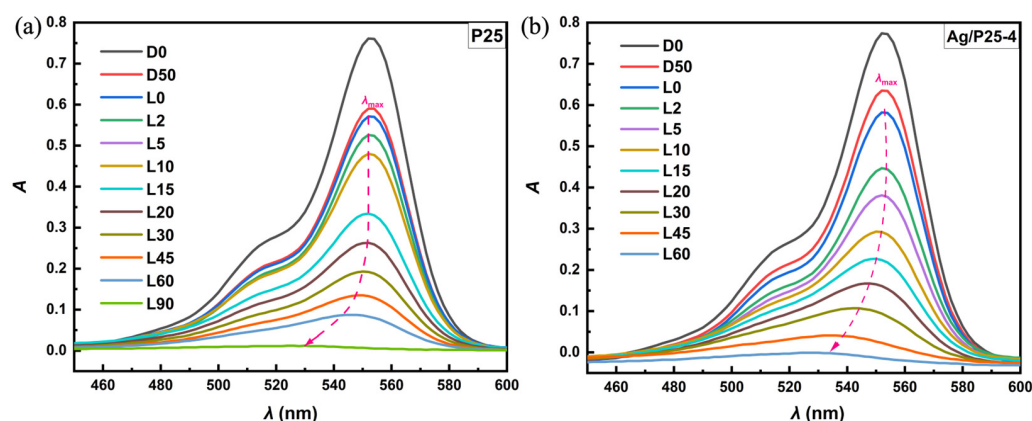

Figure 7. Absorption spectral changes of RhB solutions in the presence of (**a**) P25 and (**b**) Ag/P25-4 at given times. DX: time t = X(min) since dark reaction started; LX: time t = X(min) since Xenon light irradiation.

Other investigations have also explored the photocatalytic performance of Ag/TiO$_2$ nanocompounds in degrading RhB (shown in Table 3). For instance, Sun et al. [53] synthesized Ag-TiO$_2$ nanowire at a mole ratio of 3% (3 at%) and utilized 100 mg samples to photodegrade 200 mL RhB solution (10 mg/L), achieving complete removal of RhB in 45 min. Hajipour et al. [74] developed another variant of Ag/TiO$_2$ nanowire and utilized it to break down a 12 mg/L RhB solution, with a rate constant of 0.026 min^{-1}. In contrast, Ag/P25-6, in our study, displayed a much higher rate constant of 0.0674 min^{-1} and required less photocatalyst (30 mg) to degrade a higher concentration of RhB solution (30 mg/L), showcasing superior photocatalytic performance when compared to previous works.

The recycling stability is also an important parameter for assessing the catalysts, as high photocatalytic performance may be confronted with various risks such as the shedding of Ag NPs during degradation process, which can cause a sudden decrease in photocatalytic activities. To investigate the recycling stability, it is necessary to conduct recycling experiments. Figure 9 displays the removal percentages of RhB under different catalytic cycles. After four cycles, RhB can be completely removed with Ag/P25-6 as the catalyst under 60 min Xenon light irradiation. The result clearly indicates that Ag/P25-6 exhibited a stable recycling photodegradation performance with a high rate, suggesting its outstanding photocatalytic recycling stability.

3.3. Mechanism Clarification

The improved photocatalytic performance of Ag/P25 nanocomposites over P25 can be attributed to the enhancement of electron–hole separation and light utilization efficiency.

Under Xenon light exposure (Figure 10), the valence electrons of P25 become excited and transfer to the conduction band, and Ag NPs serve as electron traps to facilitate the electrons to participate in the reductive reaction of O_2 to O_2^-, as well as to prevent the recombination of electrons and holes [39,40]. Meanwhile, the LSPR effect of Ag NPs under visible light generates electron–hole pairs on their surface [61]. The photogenerated electrons from the LSPR effect then transfer to the conduction band of P25, creating a rich electronic state as the energy level of P25 is lower than that of Ag NPs [42]. As a result, compared to pure P25, Ag/P25 nanocomposites make better use of Xenon light, enabling photogenerated electrons to transfer and participate in the reaction, thereby significantly enhancing the photocatalytic activity.
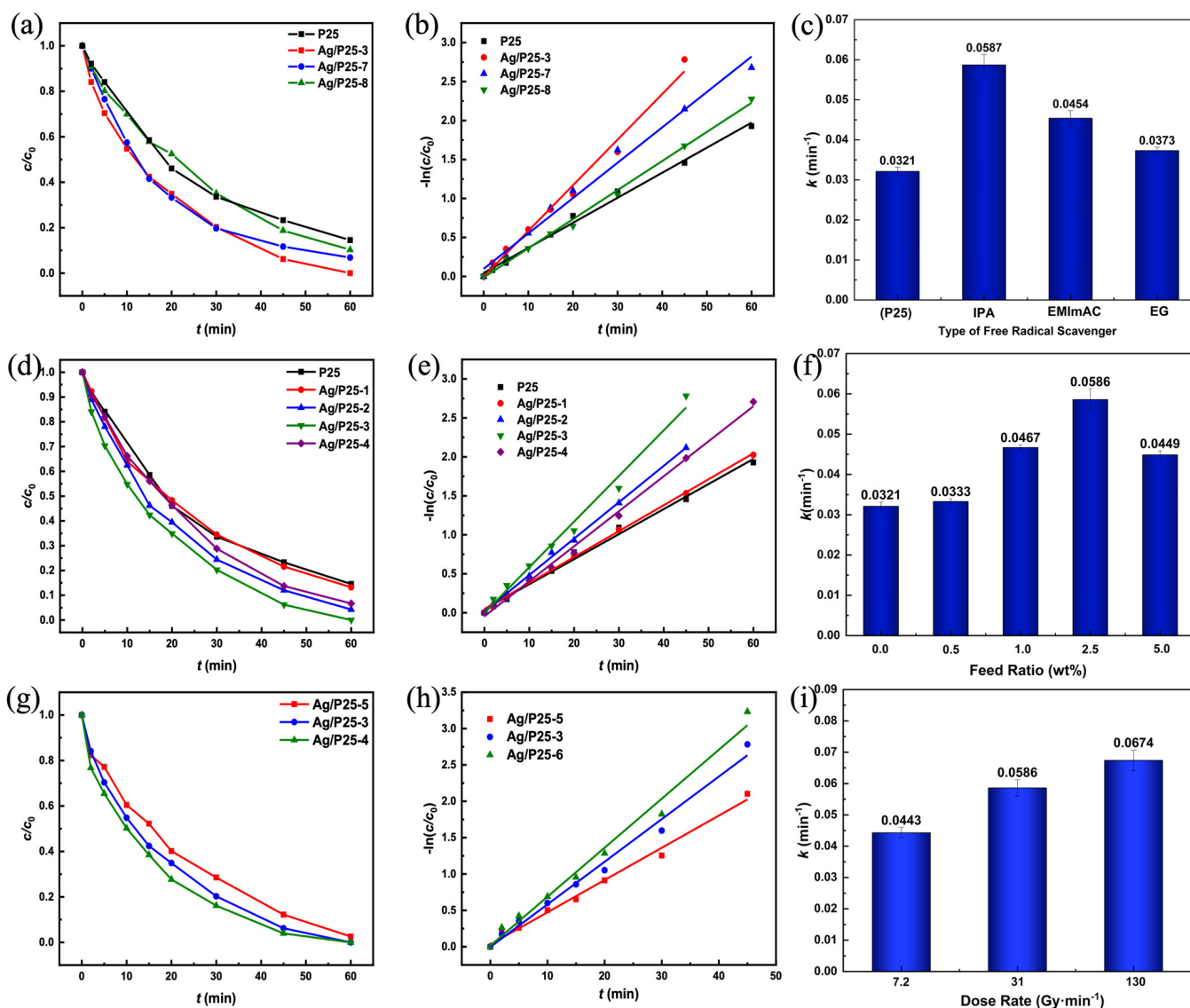

Figure 8. (**a**,**d**,**g**): Comparisons of the photocatalytic degradation curves of RhB (c/c_0 vs. irradiation time) of different Ag/P25 nanocomposites; (**b**,**e**,**h**): plots of $-\ln(c/c_0)$ versus irradiation time; (**c**,**f**,**i**): comparisons of reaction rate constants under different synthesis conditions.

In this work, Ag/P25-6, which was synthesized with a feed ratio of 2.5 wt%, an irradiation dose rate of 130 Gy/min, and IPA as the free radical scavenger, exhibited the best photocatalytic activity among all Ag/P25 nanocomposites. The impact of feed ratio on the photocatalytic performance can be explained from the perspective of electron–hole separation and recombination. A feed ratio below 2.5 wt% does not provide sufficient Ag

NPs on the surface of P25 to serve as electron traps, limiting the efficiency of electron–hole separation and reducing the reaction rate of RhB. Conversely, a high feed ratio increases the distribution density of Ag NPs on the surface of P25, causing overlapping surface plasmon resonance regions of Ag NPs, proceeding the electron–hole recombination process and reducing the reaction efficiency [42,53,75].

Table 3. Comparison with other Ag/TiO$_2$ photocatalysts.

| Photocatalysts	Preparation Method	Light Source	Reaction Solution and Amount	Removal Time and Percentage	Reaction Rate Constant (min^{-1})	Reference
Ag-1%@P25	Photo reduction	Homemade light source ($\lambda > 400$ nm, ~150 mW/cm^2)	10 mg/L, 25 mL, 50 mg	30 min, 95%	0.113(4)	[42]
3 at% Ag-TiO$_2$ nanowire	Hydrothermal process	350 W Xenon light	10 mg/L, 200 mL, 100 mg	45 min, 100%	NA	[53]
2 at% Ag-TiO$_2$ nanostructure	Hydrothermal process	800 W Xenon light ($\lambda > 420$ nm)	10 mg/L, 50 mL, 30 mg	270 min, 95%	0.01108	[54]
Ag/TiO$_2$-II	Photo reduction	500 W mercury lamp (UV)	10 mg/L, 300 mL, 600 mg	180 min, 93%	0.0144	[61]
		500 W Xenon lamp (Visible light)		180 min, 88%	0.0111	
Ag/TiO$_2$ nanowire	Polyol method	Xenon light of 75.9 kJ/m^2	12 mg/L, NA	100 min, 84%	0.026	[74]
1.0%Ag–TiO$_2$/SBA-16	Wet impregnation method	300 W Xenon light ($\lambda > 420$ nm)	10 mg/L, 100 mL, 50 mg	120 min, 90%	0.02072	[75]
Ag/P25-6	Gamma radiation reduction	300 W Xenon light	30 mg/L, 90 mL, 30 mg	45 min, 97%	0.0674	this work
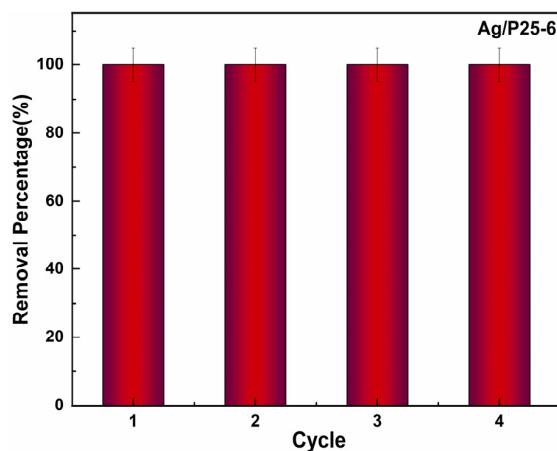
Figure 9. Recycling photocatalytic performance of Ag/P25-6 under Xenon light irradiation.
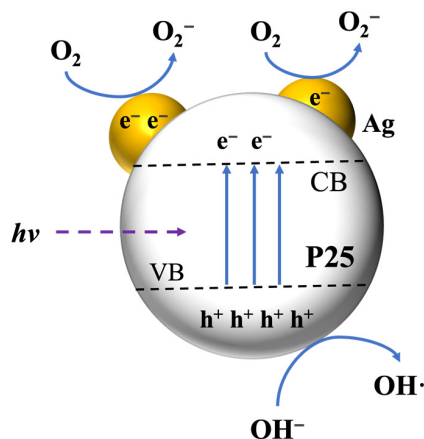

Figure 10. Schematic diagram of Ag/P25 nanocomposites for degrading RhB under Xenon light.

The influence of dose rate on the photocatalytic activity can be understood by the size of Ag NPs. From previous research by Flores-Rojas et al. [63], given a certain dose irradiation, lower dose rate induces larger particle size of Ag NPs because the production rate of reducing free radicals is slower than the association of ions with atoms. As shown in TEM image (Figure 3a–c), Ag NPs are formed in the shape of sphere, and the reduced particle sizes lead to bigger specific surface area and contact area with RhB and greatly enhance the surface-to-volume ratio of photocatalysts, which hence would improve the photocatalytic activity of Ag/P25 nanocomposites [40,47].

4. Conclusions

In summary, we have reported the successful synthesis of an efficient photocatalyst of Ag/P25 nanocomposites by utilizing a one-step gamma-ray induced reduction method in aqueous solution. The gamma-ray irradiation allowed successful doping of Ag NPs onto the surface of P25, where the dose rate had a significant impact on the size and distribution of Ag NPs, as well as the photocatalytic activity of Ag/P25 nanocomposites. Additionally, the feed ratio of Ag/P25 and the choice of free radical scavenger were found to influence the photocatalytic activity of the resulting nanocomposites. Notably, Ag/P25-6, synthesized with a feed ratio of 2.5 wt%, a dose rate of 130 Gy/min, and IPA as the free radical scavenger, exhibited a reaction rate constant 2.1 times higher than that of P25 due to its suitable load amount and small particle size. Furthermore, under Xenon light irradiation, Ag/P25 nanocomposites demonstrated superior photocatalytic activity compared to P25 due to the enhanced electron–hole separation and the extended responding range to the visible light spectrum caused by the LSPR effect. This study offers an effective method for the synthesis of Ag/TiO$_2$ nanocomposites with efficient photocatalytic performance, which could be potentially extended to the synthesis of other metal-doped semiconductor catalytic system.

Author Contributions: Conceptualization, Z.Z., S.L., X.Q. and M.Z.; methodology, Z.Z., S.L. and X.Q.; validation, J.P. and M.Z.; formal analysis, Z.Z. and S.L.; investigation, Z.Z. and S.L.; resources, J.L. and M.Z.; data curation, Z.Z., S.L. and X.Q.; writing—original draft preparation, Z.Z.; writing—review and editing, S.L., J.P. and M.Z.; visualization, Z.Z. and S.L.; supervision, J.P. and M.Z.; project administration, M.Z.; funding acquisition, M.Z. All authors have read and agreed to the published version of the manuscript.

Data Availability Statement: Not applicable.

References

1. Zhang, Y.W.; Ma, H.L.; Peng, J.; Xu, L.; Li, J.Q.; Zhai, M.L. Radiation-Induced Grafting of 4-Vinyl Pyridine onto Cellulose Microsphere for Cr(VI) Removal. *Desalin. Water Treat.* **2018**, *105*, 255–263. [CrossRef]
2. Zhang, N.; Han, C.; Fu, X.Z.; Xu, Y.J. Function-Oriented Engineering of Metal-Based Nanohybrids for Photoredox Catalysis: Exerting Plasmonic Effect and Beyond. *Chem* **2018**, *4*, 1832–1861. [CrossRef]
3. Zhang, Y.; Ma, H.L.; Cao, K.; Wang, L.; Zeng, X.; Zhang, X.; He, L.; Liu, P.; Wang, Z.; Zhai, M. Gamma Irradiation-Induced Preparation of Graphene-Ni Nanocomposites with Efficient Electromagnetic Wave Absorption. *Materials* **2018**, *11*, 2145. [CrossRef]
4. Chen, Y.; Guerin, S.; Yuan, H.; O'Donnell, J.; Xue, B.; Cazade, P.A.; Haq, E.U.; Shimon, L.J.; Rencus-Lazar, S.; Tofail, S.A.; et al. Guest Molecule-Mediated Energy Harvesting in a Conformationally Sensitive Peptide-Metal Organic Framework. *J. Am. Chem. Soc.* **2022**, *144*, 3468–3476. [CrossRef]
5. Basso Peressut, A.; Cristiani, C.; Dotelli, G.; Dotti, A.; Latorrata, S.; Bahamonde, A.; Gascó, A.; Hermosilla, D.; Balzarotti, R. Reduced Graphene Oxide/Waste-Derived TiO$_2$ Composite Membranes: Preliminary Study of a New Material for Hybrid Wastewater Treatment. *Nanomaterials* **2023**, *13*, 1043. [CrossRef] [PubMed]
6. Bolton, J.R.; Bircher, K.G.; Tumas, W.; Tolman, C.A. Figures-of-Merit for the Technical Development and Application of Advanced Oxidation Technologies for Both Electric- and Solar-Driven Systems—(IUPAC Technical Report). *Pure Appl. Chem.* **2001**, *73*, 627–637. [CrossRef]
7. Miklos, D.B.; Remy, C.; Jekel, M.; Linden, K.G.; Drewes, J.E.; Huebner, U. Evaluation of Advanced Oxidation Processes for Water and Wastewater Treatment—A Critical Review. *Water Res.* **2018**, *139*, 118–131. [CrossRef]

8. Ganiyu, S.O.; Sable, S.; El-Din, M.G. Advanced Oxidation Processes for the Degradation of Dissolved Organics in Produced Water: A Review of Process Performance, Degradation Kinetics and Pathway. *Chem. Eng. J.* **2022**, *429*, 132492. [CrossRef]

9. Ângelo, J.; Andrade, L.; Madeira, L.M.; Mendes, A. An Overview of Photocatalysis Phenomena Applied to NOx Abatement. *J. Environ. Manag.* **2013**, *129*, 522–539. [CrossRef]

10. Mills, A.; Lee, S.K. Detoxification of Water by Semiconductor Photocatalysis. *J. Ind. Eng. Chem.* **2004**, *10*, 173–187.

11. Sornalingam, K.; McDonagh, A.; Zhou, J.L.; Johir, M.A.H.; Ahmed, M.B. Photocatalysis of Estrone in Water and Wastewater: Comparison between Au-TiO$_2$ Nanocomposite and TiO$_2$, and Degradation By-Products. *Sci. Total Environ.* **2018**, *610*, 521–530. [CrossRef] [PubMed]

12. Alvillo-Rivera, A.; Garrido-Hoyos, S.; Buitron, G.; Thangarasu-Sarasvathi, P.; Rosano-Ortega, G. Biological Treatment for the Degradation of Cyanide: A Review. *J. Mater. Res. Technol.* **2021**, *12*, 1418–1433. [CrossRef]

13. Jaramillo-Fierro, X.; Leon, R. Effect of Doping TiO$_2$ NPs with Lanthanides (La, Ce and Eu) on the Adsorption and Photodegradation of Cyanide-A Comparative Study. *Nanomaterials* **2023**, *13*, 1068. [CrossRef] [PubMed]

14. Upadhyay, G.K.; Rajput, J.K.; Pathak, T.K.; Kumar, V.; Purohit, L.P. Synthesis of ZnO:TiO$_2$ Nanocomposites for Photocatalyst Application in Visible Light. *Vacuum* **2019**, *160*, 154–163. [CrossRef]

15. Smith, J.G.; Faucheaux, J.A.; Jain, P.K. Plasmon Resonances for Solar Energy Harvesting: A Mechanistic Outlook. *Nano Today* **2015**, *10*, 67–80. [CrossRef]

16. Ibhadon, A.O.; Pitzpatrick, P. Heterogeneous Photocatalysis: Recent Advances and Applications. *Catalysts* **2013**, *3*, 189–218. [CrossRef]

17. Kabra, K.; Chaudhary, R.; Sawhney, R.L. Treatment of Hazardous Organic and Inorganic Compounds through Aqueous-Phase Photocatalysis: A Review. *Ind. Eng. Chem. Res.* **2004**, *43*, 7683–7696. [CrossRef]

18. Liu, Y.; Li, Z.; Green, M.; Just, M.; Li, Y.Y.; Chen, X.B. Titanium Dioxide Nanomaterials for Photocatalysis. *J. Phys. D Appl. Phys.* **2017**, *50*, 193003. [CrossRef]

19. Zhang, Y.F.; Fu, F.; Li, Y.Z.; Zhang, D.S.; Chen, Y.Y. One-Step Synthesis of Ag@TiO$_2$ Nanoparticles for Enhanced Photocatalytic Performance. *Nanomaterials* **2018**, *8*, 1032. [CrossRef]

20. Xu, C.X.; Chen, P.W.; Liu, J.J.; Yin, H.; Gao, X.; Mei, X.F. Fabrication of Visible-Light-Driven Ag/TiO$_2$ Heterojunction Composites Induced by Shock Wave. *J. Alloys Compd.* **2016**, *679*, 463–469. [CrossRef]

21. Du, J.; Gu, X.; Guo, H.Z.; Liu, J.; Wu, Q.; Zou, J.G. Self-Induced Preparation of TiO$_2$ Nanowires by Chemical Vapor Deposition. *J. Cryst. Growth* **2015**, *427*, 54–59. [CrossRef]

22. Grover, I.S.; Prajapat, R.C.; Singh, S.; Pal, B. Highly Photoactive Au-TiO$_2$ Nanowires for Improved Photo-Degradation of Propiconazole Fungicide under UV/Sunlight Irradiation. *Sol. Energy* **2017**, *144*, 612–618. [CrossRef]

23. Tsai, C.Y.; Liu, C.W.; Hsi, H.C.; Lin, K.S.; Lin, Y.W.; Lai, L.C. Synthesis of Ag-Modified TiO$_2$ Nanotube and its Application in Photocatalytic Degradation of Dyes and Elemental Mercury. *J. Chem. Technol. Biotechnol.* **2019**, *94*, 3251–3262. [CrossRef]

24. Kang, S.; Choi, J.; Park, G.Y.; Kim, H.R.; Hwang, J. A Novel and Facile Synthesis of Ag-Doped TiO$_2$ Nanofiber for Airborne Virus/Bacteria Inactivation and VOC Elimination under Visible Light. *Appl. Surf. Sci.* **2022**, *599*, 153930. [CrossRef]

25. Kanmoni, V.G.G.; Daniel, S.; Raj, G.A.G. Photocatalytic Degradation of Chlorpyrifos in Aqueous Suspensions Using Nanocrystals of ZnO and TiO$_2$. *React. Kinet. Mech. Catal.* **2012**, *106*, 325–339. [CrossRef]

26. Guo, C.S.; Xu, J.A.; He, Y.; Zhang, Y.A.; Wang, Y.Q. Photodegradation of Rhodamine B and Methyl Orange over One-Dimensional TiO$_2$ Catalysts under Simulated Solar Irradiation. *Appl. Surf. Sci.* **2011**, *257*, 3798–3803. [CrossRef]

27. Jovic, V.; Chen, W.T.; Sun-Waterhouse, D.; Blackford, M.G.; Idriss, H.; Waterhouse, G.I.N. Effect of Gold Loading and TiO$_2$ Support Composition on the Activity of Au/TiO$_2$ Photocatalysts for H$_2$ Production from Ethanol-Water Mixtures. *J. Catal.* **2013**, *305*, 307–317. [CrossRef]

28. Hu, S.; Shaner, M.R.; Beardslee, J.A.; Lichterman, M.; Brunschwig, B.S.; Lewis, N.S. Amorphous TiO$_2$ Coatings Stabilize Si, GaAs, and GaP Photoanodes for Efficient Water Oxidation. *Science* **2014**, *344*, 1005–1009. [CrossRef]

29. Cao, X.B.; Lu, Z.F.; Zhu, L.W.; Yang, L.; Gu, L.; Cai, L.L.; Chen, J. A New Family of Sunlight-Driven Bifunctional Photocatalysts Based on TiO$_2$ Nanoribbon Frameworks and Bismuth Oxohalide Nanoplates. *Nanoscale* **2014**, *6*, 1434–1444. [CrossRef]

30. Hossain, M.K.; Mortuza, A.A.; Sen, S.K.; Basher, M.K.; Ashraf, M.W.; Tayyaba, S.; Mia, M.N.H.; Uddin, M.J. A Comparative Study on the Influence of Pure Anatase and Degussa-P25 TiO$_2$ Nanomaterials on the Structural and Optical Properties of Dye Sensitized Solar Cell (DSSC) Photoanode. *Optik* **2018**, *171*, 507–516. [CrossRef]

31. Lincho, J.; Zaleska-Medynska, A.; Martins, R.C.; Gomes, J. Nanostructured Photocatalysts for the Abatement of Contaminants by Photocatalysis and Photocatalytic Ozonation: An Overview. *Sci. Total Environ.* **2022**, *837*, 155776. [CrossRef] [PubMed]

32. Elleuch, L.; Messaoud, M.; Djebali, K.; Attafi, M.; Cherni, Y.; Kasmi, M.; Elaoud, A.; Trabelsi, I.; Chatti, A. A New Insight into Highly Contaminated Landfill Leachate Treatment Using Kefir Grains Pre-Treatment Combined with Ag-Doped TiO$_2$ Photocatalytic Process. *J. Hazard. Mater.* **2019**, *382*, 121119. [CrossRef] [PubMed]

33. Komatsuda, S.; Asakura, Y.; Vequizo, J.J.M.; Yamakata, A.; Yin, S. Enhanced Photocatalytic NO$_x$ Decomposition of Visible-Light Responsive F-TiO$_2$/(N,C)-TiO$_2$ by Charge Transfer Between F-TiO$_2$ and (N,C)-TiO$_2$ through their Doping Levels. *Appl. Catal. B Environ.* **2018**, *238*, 358–364. [CrossRef]

34. Kou, J.H.; Lu, C.H.; Wang, J.; Chen, Y.K.; Xu, Z.Z.; Varma, R.S. Selectivity Enhancement in Heterogeneous Photocatalytic Transformations. *Chem. Rev.* **2017**, *117*, 1445–1514. [CrossRef]

35. Gao, X.H.; Zhou, B.H.; Yuan, R.F. Doping a Metal (Ag, Al, Mn, Ni and Zn) on TiO_2 Nanotubes and its Effect on Rhodamine B Photocatalytic Oxidation. *Environ. Eng. Res.* **2015**, *20*, 329–335. [CrossRef]

36. Belver, C.; Hinojosa, M.; Bedia, J.; Tobajas, M.; Alvarez, M.A.; Rodriguez-Gonzalez, V.; Rodriguez, J.J. Ag-Coated Heterostructures of ZnO-TiO_2/Delaminated Montmorillonite as Solar Photocatalysts. *Materials* **2017**, *10*, 960. [CrossRef]

37. Liu, S.Q.; Zhang, N.; Tang, Z.R.; Xu, Y.J. Synthesis of One-Dimensional CdS@TiO_2 Core-Shell Nanocomposites Photocatalyst for Selective Redox: The Dual Role of TiO_2 Shell. *ACS Appl. Mater. Interfaces* **2012**, *4*, 6378–6385. [CrossRef]

38. Low, J.X.; Dai, B.Z.; Tong, T.; Jiang, C.J.; Yu, J.G. In Situ Irradiated X-Ray Photoelectron Spectroscopy Investigation on a Direct Z-Scheme TiO_2/CdS Composite Film Photocatalyst. *Adv. Mater.* **2019**, *31*, 1802981. [CrossRef]

39. Sung-Suh, H.M.; Choi, J.R.; Hah, H.J.; Koo, S.M.; Bae, Y.C. Comparison of Ag Deposition Effects on the Photocatalytic Activity of Nanoparticulate TiO_2 under Visible and UV Light Irradiation. *J. Photochem. Photobiol. A Chem.* **2004**, *163*, 37–44. [CrossRef]

40. Liu, S.H.; Huang, G.; Wang, J.F.; Bao, J.S.; Wang, M.Y.; Wei, Y.Q.; Zhong, Y.; Bai, F. Noble Metal Nanoparticle-Loaded Porphyrin Hexagonal Submicrowires Composites (M-HW): Photocatalytic Synthesis and Enhanced Photocatalytic Activity. *Nanomaterials* **2023**, *13*, 660. [CrossRef]

41. Liu, L.Q.; Zhang, X.N.; Yang, L.F.; Ren, L.T.; Wang, D.F.; Ye, J.H. Metal Nanoparticles Induced Photocatalysis. *Natl. Sci. Rev.* **2017**, *4*, 761–780. [CrossRef]

42. Chen, D.; Chen, Q.; Ge, L.; Yin, L.; Fan, B.; Wang, H.; Lu, H.; Xu, H.; Zhang, R.; Shao, G. Synthesis and Ag-Loading-Density-Dependent Photocatalytic Activity of Ag@TiO_2 Hybrid Nanocrystals. *Appl. Surf. Sci.* **2013**, *284*, 921–929. [CrossRef]

43. Huang, P.S.; Qin, F.; Lee, J.K. Role of the Interface between Ag and ZnO in the Electric Conductivity of Ag Nanoparticle-Embedded ZnO. *ACS Appl. Mater. Interfaces* **2020**, *12*, 4715–4721. [CrossRef]

44. Wu, Y.Y.; Zhang, L.L.; Zhou, Y.Z.; Zhang, L.L.; Li, Y.; Liu, Q.Q.; Hu, J.; Yang, J. Light-Induced ZnO/Ag/rGO Bactericidal Photocatalyst with Synergistic Effect of Sustained Release of Silver Ions and Enhanced Reactive Oxygen Species. *Chin. J. Catal.* **2019**, *40*, 691–702. [CrossRef]

45. Ou, W.H.; Shen, J.D.; Lyu, F.C.; Xiao, X.F.; Zhou, B.B.; Lu, J.; Li, Y.Y. Facile Surfactant-, Reductant-, and Ag Salt-Free Growth of Ag Nanoparticles with Controllable Size from 35 to 660 nm on Bulk Ag Materials. *Chem.-Asian J.* **2021**, *16*, 2249–2252. [CrossRef]

46. Ruan, W.; Cui, Y.; Lin, F.; Zhou, T.; Hui, G.; Wang, Y.; Chen, Y.; Lu, F.; Guo, J.; Zhao, B. Fabrication of Periodical Ag-Au Compound Nanostructure Films with Controllable Ag Nanoparticle Aggregate Patterns: A Study on Surface-Enhanced Raman Scattering. *J. Raman Spectrosc.* **2015**, *46*, 1117–1123. [CrossRef]

47. Ma, J.Y.; Tan, X.J.; Zhang, Q.Q.; Wang, Y.; Zhang, J.L.; Wang, L.Z. Exploring the Size Effect of Pt Nanoparticles on the Photocatalytic Nonoxidative Coupling of Methane. *ACS Catal.* **2021**, *11*, 3352–3360. [CrossRef]

48. Abdelghany, A.M.; Abdelrazek, E.M.; Badr, S.I.; Abdel-Aziz, M.S.; Morsi, M.A. Effect of Gamma-Irradiation on Biosynthesized Gold Nanoparticles Using *Chenopodium Murale* Leaf Extract. *J. Saudi Chem. Soc.* **2017**, *21*, 528–537. [CrossRef]

49. Que, X.; Lin, T.; Li, S.; Chen, X.; Hu, C.; Wang, Y.; Shi, M.; Peng, J.; Li, J.; Ma, J.; et al. Radiation Synthesis of Size-Controllable Ruthenium-Based Electrocatalysts for Hydrogen Evolution Reaction. *Appl. Surf. Sci.* **2021**, *541*, 148345–148352. [CrossRef]

50. Mahdieh, Z.M.; Shekarriz, S.; Taromi, F.A.; Montazer, M. A New Method for in situ Synthesis of Ag-TiO_2 Nanocomposite Particles on Polyester/Cellulose Fabric by Photoreduction and Self-Cleaning Properties. *Cellulose* **2018**, *25*, 2355–2366. [CrossRef]

51. Lenzi, G.G.; Favero, C.V.B.; Colpini, L.M.S.; Bernabe, H.; Baesso, M.L.; Specchia, S.; Santos, O.A.A. Photocatalytic Reduction of Hg(II) on TiO_2 and Ag/TiO_2 Prepared by the Sol-Gel and Impregnation Methods. *Desalination* **2011**, *270*, 241–247. [CrossRef]

52. Liu, R.R.; Ji, Z.J.; Wang, J.; Zhang, J.J. Solvothermal Synthesized Ag-Decorated TiO_2/Sepiolite Composite with Enhanced UV-Vis and Visible Light Photocatalytic Activity. *Micropor. Mesopor. Mater.* **2018**, *266*, 268–275. [CrossRef]

53. Sun, Y.; Gao, Y.; Zeng, J.Y.; Guo, J.; Wang, H. Enhancing Visible-Light Photocatalytic Activity of Ag-TiO_2 Nanowire Composites by One-Step Hydrothermal Process. *Mater. Lett.* **2020**, *279*, 128506–128510. [CrossRef]

54. Zhang, Y.; Wang, T.; Zhou, M.; Wang, Y.; Zhang, Z.M. Hydrothermal Preparation of Ag-TiO_2 Nanostructures with Exposed {001}/{101} Facets for Enhancing Visible Light Photocatalytic Activity. *Ceram. Int.* **2017**, *43*, 3118–3126. [CrossRef]

55. Wang, C.L.; Yang, K.; Wei, X.H.; Ding, S.; Tian, F.; Li, F. One-pot solvothermal synthesis of carbon dots/Ag nanoparticles/TiO_2 nanocomposites with enhanced photocatalytic performance. *Ceram. Int.* **2018**, *44*, 22481–22488. [CrossRef]

56. Zhang, L.X.; Ni, C.H.; Jiu, H.F.; Xie, C.M.; Yan, J.B.; Qi, G.S. One-pot synthesis of Ag-TiO_2/reduced graphene oxide nanocomposite for high performance of adsorption and photocatalysis. *Ceram. Int.* **2017**, *43*, 5450–5456. [CrossRef]

57. Di, L.B.; Xu, Z.J.; Zhang, X.L. Atmospheric-Pressure Cold Plasma for Synthesizing Ag Modified Degussa P25 with Visible Light Activity Using Dielectric Barrier Discharge. *Catal. Today* **2013**, *211*, 143–146. [CrossRef]

58. Dong, P.M.; Nie, X.X.; Jin, Z.; Huang, Z.F.; Wang, X.Y.; Zhang, X.W. Dual Dielectric Barrier Discharge Plasma Treatments for Synthesis of Ag-TiO_2 Functionalized Polypropylene Fabrics. *Ind. Eng. Chem. Res.* **2019**, *58*, 7734–7741. [CrossRef]

59. Cheng, X.D.; Dong, P.M.; Huang, Z.F.; Zhang, Y.Z.; Chen, Y.; Nie, X.X.; Zhang, X.W. Green Synthesis of Plasmonic Ag Nanoparticles Anchored TiO_2 Nanorod Arrays Using Cold Plasma for Visible-Light-Driven Photocatalytic Reduction of CO_2. *J. CO2 Util.* **2017**, *20*, 200–207. [CrossRef]

60. Dong, P.M.; Yang, F.F.; Cheng, X.D.; Huang, Z.F.; Nie, X.X.; Xiao, Y.H.; Zhang, X.W. Plasmon enhanced photocatalytic and antimicrobial activities of Ag-TiO_2 nanocomposites under visible light irradiation prepared by DBD cold plasma treatment. *Mater. Sci. Eng. C* **2019**, *96*, 197–204. [CrossRef]

61. Liang, H.J.; Jia, Z.C.; Zhang, H.C.; Wang, X.B.; Wang, J.J. Photocatalysis Oxidation Activity Regulation of Ag/TiO_2 Composites Evaluated by the Selective Oxidation of Rhodamine B. *Appl. Surf. Sci.* **2017**, *422*, 1–10. [CrossRef]

62. Zhou, B.; Hong, H.T.; Zhang, H.F.; Yu, S.S.; Tian, H.W. Heterostructured Ag/g-C$_3$N$_4$/TiO$_2$ with enhanced visible light photocatalytic performances. *J. Chem. Technol. Biotechnol.* **2019**, *94*, 3806–3814. [CrossRef]

63. Flores-Rojas, G.G.; Lopez-Saucedo, F.; Bucio, E. Gamma-Irradiation Applied in the Synthesis of Metallic and Organic Nanoparticles: A Short Review. *Radiat. Phys. Chem.* **2020**, *169*, 107962–107977. [CrossRef]

64. Belloni, J.; Marignier, J.L.; Mostafavi, M. Mechanisms of Metal Nanoparticles Nucleation and Growth Studied by Radiolysis. *Radiat. Phys. Chem.* **2020**, *169*, 107952. [CrossRef]

65. Rojas, J.V.; Castano, C.H. Production of Palladium Nanoparticles Supported on Multiwalled Carbon Nanotubes by Gamma Irradiation. *Radiat. Phys. Chem.* **2012**, *81*, 16–21. [CrossRef]

66. Sanchez-Polo, M.; Lopez-Penalver, J.; Prados-Joya, G.; Ferro-Garcia, M.A.; Rivera-Utrilla, J. Gamma Irradiation of Pharmaceutical Compounds, Nitroimidazoles, as a New Alternative for Water Treatment. *Water Res.* **2009**, *43*, 4028–4036. [CrossRef]

67. Fu, X.; Zhang, Y.; Cao, P.; Ma, H.; Liu, P.; He, L.; Peng, J.; Li, J.; Zhai, M. Radiation Synthesis of CdS/Reduced Graphene Oxide Nanocomposites for Visible-Light-Driven Photocatalytic Degradation of Organic Contaminant. *Radiat. Phys. Chem.* **2016**, *123*, 79–86. [CrossRef]

68. Kozmer, Z.; Takacs, E.; Wojnarovits, L.; Alapi, T.; Hernadi, K.; Dombi, A. The Influence of Radical Transfer and Scavenger Materials in Various Concentrations on the Gamma Radiolysis of Phenol. *Radiat. Phys. Chem.* **2016**, *124*, 52–57. [CrossRef]

69. Wang, S.; Zhang, Y.; Ma, H.L.; Zhang, Q.; Xu, W.; Peng, J.; Li, J.; Yu, Z.Z.; Zhai, M. Ionic-Liquid-Assisted Facile Synthesis of Silver Nanoparticle-Reduced Graphene Oxide Hybrids by Gamma Irradiation. *Carbon* **2013**, *55*, 245–252. [CrossRef]

70. Murdoch, M.; Waterhouse, G.I.N.; Nadeem, N.A.; Metson, J.B.; Keane, M.A.; Howe, R.F.; Llorca, J.; Idriss, H. The Effect of Gold Loading and Particle Size on Photocatalytic Hydrogen Production from Ethanol over Au/TiO$_2$ Nanoparticles. *Nat. Chem.* **2011**, *3*, 489–492. [CrossRef]

71. UV-Vis-NIR Spectrum for Calculation of Bandgap. Available online: https://iscms.westlake.edu.cn/info/1052/1436.htm (accessed on 25 April 2023).

72. Wang, Y.; Feng, C.X.; Zhang, M.; Yang, J.J.; Zhang, Z.J. Visible Light Active N-Doped TiO$_2$ Prepared from Different Precursors: Origin of the Visible Light Absorption and Photoactivity. *Appl. Catal. B Environ.* **2011**, *104*, 268–274. [CrossRef]

73. Natarajan, T.S.; Thomas, M.; Natarajan, K.; Bajaj, H.C.; Tayade, R.J. Study on UV-LED/TiO$_2$ Process for Degradation of Rhodamine B Dye. *Chem. Eng. J.* **2011**, *169*, 126–134. [CrossRef]

74. Hajipour, P.; Bahrami, A.; Mehr, M.Y.; van Driel, W.D.; Zhang, K.C. Facile Synthesis of Ag Nanowire/TiO$_2$ and Ag Nanowire/TiO$_2$/GO Nanocomposites for Photocatalytic Degradation of Rhodamine B. *Materials* **2021**, *14*, 763. [CrossRef] [PubMed]

75. Ma, J.; Xu, S.Y.; Chu, J.; Xue, J.Q.; Tang, J.L.; Qiang, L.S. Effect of Metal-Support Interaction on the Structural and Enhanced Photocatalytic Performance of Mesoporous M-TiO$_2$/SBA-16 (M = Ag and Fe). *J. Porous Mater.* **2017**, *24*, 45–54. [CrossRef]